# Biomedical Photonics HANDBOOK

**Editor-in-Chief**
**Tuan Vo-Dinh**


CRC PRESS

Boca Raton London New York Washington, D.C.

**Cover Art**: *Field of Lights*, oil painting by Kim-Chi Le Vo-Dinh. Reproduced with permission of the artist.

**Library of Congress Cataloging-in-Publication Data**

Biomedical photonics handbook / edited by Tuan Vo-Dinh.
p. cm.
Includes bibliographical references and index.
ISBN 0-8493-1116-0
1. Optoelectronic devices—Handbooks, manuals, etc. 2. Biosensors—Handbooks, manuals, etc. 3. Diagnositic imaging—Handbooks, manuals, etc. 4. Imaging systems in medicine—Handbooks, manuals, etc. I. Vo-Dinh, Tuan.

R857.06 B573 2002
610′.28—dc21 2002034914



**Visit the CRC Press Web site at www.crcpress.com**


International Standard Book Number 0-8493-1116-0
Library of Congress Card Number 2002034914
Printed in the United States of America 1 2 3 4 5 6 7 8 9 0
Printed on acid-free paper

# 21

# Functional Imaging with Diffusing Light


21.1 Introduction ..... 21-1
21.2 Theory ..... 21-3
Diffusion Approximation • Sources of Diffusing Photons • Diffuse Photon Density Waves in Homogeneous Turbid Media • Spectroscopy of Homogeneous Turbid Media • Imaging in Heterogeneous Media • Diffusion of Light Correlations: Blood Flow • Contrast Agents
21.3 Instrumentation ..... 21-15
Source Encoding Strategies
21.4 Experimental Diffuse Optical Tomography: Functional Breast and Brain Imaging ..... 21-18
Multiple Absorbers in a Slab Phantom • Breast Imaging • Diffuse Optical Imaging of Brain Function
21.5 Fundamental and Practical Issues: Problems and Solutions ..... 21-30
Detection, Localization, Characterization, and Resolution Limits • Calibration of Source and Detector Amplitudes
Acknowledgments ..... 21-33
References ..... 21-33



Arjun G. Yodh
*University of Pennsylvania*
*Philadelphia, Pennsylvania*

David A. Boas
*Harvard Medical School*
*Massachusetts General Hospital*
*Athinoula A. Martinos Center for Biomedical Imaging*
*Charlestown, Massachusetts*


## 21.1 Introduction

Many materials are visually opaque because photons traveling within them are predominantly scattered rather than absorbed. Some common examples of these highly scattering media include white paint, foam, mayonnaise, and human tissue. Indeed, anyone who has held a flashlight up to his or her hand will notice some of this light is transmitted, albeit after experiencing many scattering events. Light travels through these materials in a process similar to heat diffusion.

What does it mean to say light transport is diffusive? Consider a simple experiment in which an optical fiber is used to inject light into a highly scattering material such as paint or tissue. Microscopically, the injected photons experience thousands of elastic scattering events in the media. A few of the photons will be absorbed by chromophores and will be lost. The remaining photons travel along pathways that resemble a random walk. These individual trajectories are composed of straight-line segments with sudden interruptions where the photon propagation direction is randomly changed. The average length of the straight-line segments is called the random walk steplength of the traveling photon. By summing all trajectories one can compute the photon concentration or photon fluence rate as a function of time and position within the media.

It is then straightforward to show that the collective migration of photon concentration is described by a diffusion equation. In practice one can carry out a variety of measurements to confirm the diffusive


0-8493-1116-0/03/$0.00+$1.50

nature of light transport. For example, if a short pulse of light is injected into the medium and a second optical fiber is used to detect transmitted photons, then, when the transport is diffusive, the most probable arrival times for the detected photons will scale with the square of the source-detector separation divided by the random walk steplength.

Diffuse light imaging and spectroscopy aims to investigate tissue physiology millimeters to centimeters below the tissue surface.[1–5] The cost of this goal is that we must abandon traditional optical spectroscopies and traditional microscopy because traditional methodologies require optically thin samples. In addition, light penetration must be large in order to reach tissue located centimeters below the surface. Fortunately, a spectral window exists within tissues in the near-infrared from 700 to 900 nm, wherein photon transport is dominated by scattering rather than absorption. The absorption of hemoglobin and water is small in the near-infrared, but elastic scattering from organelles and other microscopic interfaces is large. These are precisely the conditions required for application of the diffusion model. The recognition and widespread acceptance that light transport over long distances in tissues is well approximated as a diffusive process has propelled the field. Using this physical model it is possible to separate tissue scattering from tissue absorption quantitatively, and to incorporate the influence of boundaries, such as the air-tissue interface, into the transport theory accurately. The diffusion approximation also provides a tractable basis for tomographic approaches to image reconstruction using highly scattered light. Tomographic methods were not employed in early transillumination patient studies, and are crucial for recovery of information about tissue optical property heterogeneity.

Even though absorption in the near-infrared is relatively small, the spectra of major tissue chromophores, particularly oxy- and deoxyhemoglobin and water, differ significantly in the near-infrared. As a result, the diffuse optical methods are sensitive to blood dynamics, blood volume, blood oxygen saturation, and water and lipid content of interrogated tissues. In addition, one can induce optical contrast in tissues with exogenous contrast agents, for example, chemical species that occupy vascular and extravascular space and preferentially accumulate in diseased tissue. Together these sensitivities provide experimenters with access to a wide spectrum of biophysical problems. The greater blood supply and metabolism of tumors compared to surrounding tissues provides target heterogeneity for tissue maps based on absorption.[6–25] Similar maps can be applied for studies of brain bleeding[26–28] and cerebral oxygen dynamics associated with activation by mental and physical stimulation.[29–41] Other applications of the deep tissue methods include the study of mitochondrial diseases,[42–44] of muscle function and physiology,[45,46] and of photodynamic therapy.[47–51]

Biomedical applications for diffusing near-infrared light probes parallel the application of nuclear magnetic resonance to tissue study. Generally, the categories of measurement can be termed spectroscopy and imaging. Spectroscopy is useful for measurement of time-dependent variations in the absorption and scattering of large tissue volumes. For example, brain oximetry (hemoglobin spectroscopy) of the frontal, parietal, or occipital regions can reveal reduced brain perfusion caused by head injury. Imaging is important when a localized heterogeneity of tissue is involved, for example, an early breast or brain tumor, a small amount of bleeding in the brain, or an early aneurysm. Images enable one to identify the site of the trauma and differentiate it from background tissue. Imaging is also important because it improves the accuracy of a spectroscopic measurement. Typically, spectroscopic methods employ oversimplified assumptions about the scattering media. Imaging relaxes some of these assumptions, usually at the cost of a more complex experimental instrument and computation, and ultimately improves the fidelity of the gathered optical property information.

The purpose of this chapter is to discuss functional imaging with diffusing photons. Our emphasis will be on imaging rather than spectroscopy, but it will be necessary to briefly review the basics of diffuse optical spectroscopy. This chapter is intended as a tutorial about what can be done with diffuse optical imaging, how to do it, and how to understand it. We intend to give a tutorial snapshot of the field with selected examples, but not a comprehensive review of research in the field. The remainder of this tutorial consists of sections on theory, instrumentation, and imaging examples, and a discussion about limitations and compromises associated with the technique.

## 21.2 Theory

### 21.2.1 Diffusion Approximation

Many researchers (e.g., References 52 through 56 and others) have shown that the photon fluence rate, $\Phi(\mathbf{r}, t)$ (photons/[cm$^2$ · s]), obeys the following diffusion equation in highly scattering media:

$$\nabla \cdot D(\mathbf{r})\nabla\Phi(\mathbf{r},t) - v\mu_a(\mathbf{r})\Phi(\mathbf{r},t) + vS(\mathbf{r},t) = \frac{\partial\Phi(\mathbf{r},t)}{\partial t}. \tag{21.1}$$

$\Phi(\mathbf{r},t)$ is proportional to the photon number density $U(\mathbf{r}, t)$ (photons/cm$^3$), i.e., $\Phi(\mathbf{r}, t) = vU(\mathbf{r}, t)$. The turbid medium is characterized by a speed of light, $v$, an absorption coefficient $\mu_a$ (i.e., the multiplicative inverse of the photon absorption length), and a photon diffusion coefficient, $D = v/3(\mu_s' + \mu_a) \equiv v/3(\mu_s')$; the dependence of $D$ on $\mu_a$ is a subject of recent debate,[53, 57–68] but the latter relation follows in most tissues wherein $\mu_s' >> \mu_a$. The medium's reduced scattering coefficient is defined as $\mu_s' = (1 - g)\,\mu_s$ and represents the multiplicative inverse of the photon random walk steplength, $l^*$. Here $\mu_s$ is the reciprocal of the photon scattering length, $l$, and $g = \langle\cos\theta\rangle$ is the ensemble-averaged cosine of the scattering angle $\theta$ associated with a typical single scattering event in the sample; $g$ accounts for the fact that light is more typically scattered in the forward direction, so that many scattering events are required before the initial photon propagation direction is truly randomized. $S(r, t)$ is an isotropic source term that gives the number of photons emitted at position $r$ and time $t$ per unit volume per unit time.

The right-hand side of Equation 21.1 represents the rate of increase of photons within a sample volume element. This rate equals the number of photons scattered into the volume element per unit time from its surroundings, *minus* the number of photons absorbed per unit time within the volume element, *plus* the number of photons emitted per unit time from any sources in the volume element.

The diffusion equation is based upon the $P1$ approximation of the linear transport equation.[69,70] It is valid when the reduced albedo $\alpha' = \mu_s'/(\mu_a + \mu_s')$ is close to unity, i.e., the reduced scattering coefficient is much greater than the absorption coefficient ($\mu_s' >> \mu_a$). The near-infrared (NIR) spectral window (commonly called the "therapeutic" window) of biological tissue lies between the intense visible absorption bands of hemoglobin and the NIR absorption band of water. In this window the reduced scattering coefficient is often 10 to 1000 times greater than the absorption coefficient,[71] for example, $\mu_s' = 10$ cm$^{-1}$ and $\mu_a = 0.03$ cm$^{-1}$ at 800 nm in human breast tissues. Of course tissues are not homogeneous, but they can be accurately divided into domains of piecewise homogeneous turbid media, each obeying Equation 21.1. Measurements are accomplished using sources and detectors arranged on the surfaces of or embedded within the tissue. Strictly speaking, it is also important for the source-detector separation to be of order three photon random walk steps (i.e., $3l^*$) or larger; otherwise the photon scattering angles will not be sufficiently randomized at the point of detection for rigorous application of the diffusion approximation.[72,73]

### 21.2.2 Sources of Diffusing Photons

Three types of sources are commonly employed in diffusive light measurements (see Figure 21.1). The simplest and easiest method to use is the continuous-wave (CW) device. In this case the source amplitude is constant, and the transmitted amplitude is measured as a function of source-detector separation or wavelength. The second method is the pulsed-time or time-resolved technique. In this scheme a short, usually subnanosecond light pulse is launched into the medium, and the temporal point spread function of the transmitted pulse is measured. The third method is the intensity modulated or frequency-domain technique. In this case the amplitude of the input source is sinusoidally modulated, producing a diffusive wave within the medium. The amplitude and phase of the transmitted diffuse light wave are then measured. These methods are related; the time-resolved and frequency-domain approaches are Fourier

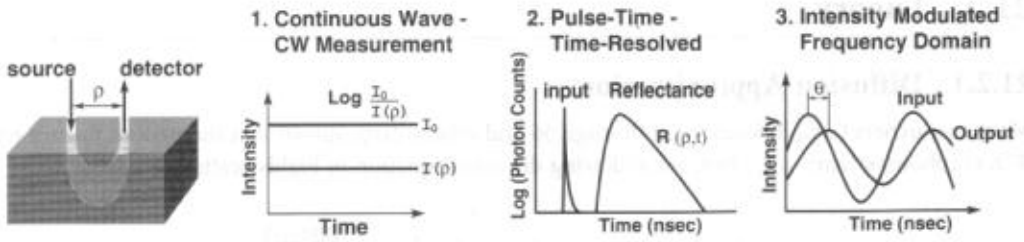


FIGURE 21.1 Three source-detector schemes are generally employed in the photon migration field. On the far left we illustrate a typical remission geometry: (1) continuous-wave, called CW spectroscopy; (2) time-pulsed or time-resolved technique (often called TRS); (3) intensity amplitude modulation, i.e., often referred to as the frequency-domain method.

transformations of one another, and the CW approach is a special case of the frequency-domain approach wherein the modulation frequency is zero. Each of these approaches has strengths and weaknesses.

Briefly, the CW scheme is inexpensive and provides for rapid data collection. However, because it measures amplitude only, it lacks the capability for characterizing simultaneously the absorption and scattering of even a homogeneous medium from a measurement using only a single source-detector pair. The more expensive time-resolved scheme collects the full temporal point spread function, which is equivalent to a frequency domain measurement over a wide range of modulation frequencies. In this case, when the medium is homogeneous, $\mu_a$ and $\mu_s'$ can be obtained simultaneously from a single source-detector separation. The photon counting, however, can be slow and the technique is often limited by shot noise. The frequency domain technique is a compromise between CW and time-resolved techniques, with respect to cost and speed. It concentrates all the light energy into a single modulation frequency. It measures amplitude and phase, which ideally enable us to obtain $\mu_a$ and $\mu_s'$ for a homogeneous medium using a single source-detector separation. In practice all of these methods benefit significantly from use of many source-detector pairs and many optical wavelengths. In this chapter we focus on frequency domain sources, but the results can be applied to time-resolved and CW methods.

### 21.2.3 Diffuse Photon Density Waves in Homogeneous Turbid Media

Consider a light source at the origin with its intensity sinusoidally modulated at a modulation frequency $f$, e.g., the source term in Equation 21.1 is $S(\mathbf{r},t) = (M_{dc} + M_{ac}e^{-i\omega t})\,\delta(\mathbf{r})$, where $\omega = 2\pi f$ is the angular source modulation frequency, $M_{dc}$ and $M_{ac}$ are the source strengths of the DC and AC source components. The diffusion equation continues to be valid for light derived from these highly modulated sources as long as the modulation frequency $\omega$ is significantly smaller than the scattering frequency $v\mu_s'$; that is, photons must experience many scattering events during a single modulation period. Photons leaving the source and traveling along different random walk trajectories within the turbid medium will add incoherently to form a macroscopic scalar wave of photon concentration or fluence rate.

The total fluence rate consists of a DC and an AC component, i.e., $\Phi_{total}(\mathbf{r},t) = \Phi_{DC}(\mathbf{r}) + \Phi_{AC}(\mathbf{r}, t)$. We focus on the AC component $\Phi_{AC}(\mathbf{r},t) = \Phi(\mathbf{r})e^{-i\omega t}$. The photon fluence will oscillate at the source of modulation frequency $\omega$. Plugging the AC source term into Equation 21.1 we obtain the following Helmholtz equation for the oscillating part of the photon fluence:

$$\left(\nabla^2 + k^2\right)\Phi(\mathbf{r}) = -\left(\frac{vM_{ac}}{D}\right)\delta(\mathbf{r}). \tag{21.2}$$

We refer to this disturbance as a diffuse photon density wave (DPDW).[74,75] The DPDW has wavelike properties; for example, refractive,[76] diffractive,[77] and dispersive[78] behaviors of the DPDW have been demonstrated.

The photon density wave has a simple spherical wave solution for an infinite homogeneous highly scattering medium of the form:

$$\Phi_{AC}(\mathbf{r},t)=\left(\frac{vM_{ac}}{4\pi Dr}\right)\exp(ikr)\exp(-i\omega t). \tag{21.3}$$

The diffuse photon density wave wavenumber is complex, $k = k_r + ik_i$, and $k^2 = (-v\mu_a + i\omega)/D$. The real and imaginary parts of the wavenumber are:

$$k_r=\left(\frac{v\mu_a}{2D}\right)^{1/2}\left(\left(1+\left(\frac{\omega^2}{v\mu_a}\right)\right)^{1/2}-1\right)^{1/2}$$
$$k_i=\left(\frac{v\mu_a}{2D}\right)^{1/2}\left(\left(1+\left(\frac{\omega^2}{v\mu_a}\right)\right)^{1/2}+1\right)^{1/2}. \tag{21.4}$$

In Figure 21.2 the measured wave is demonstrated within a tank of homogeneous highly scattering Intralipid. Constant-phase contours are shown in 20° intervals about the source at the origin. We see that the wave contours are circular and that their radii can be extrapolated back to the source. In the inset we exhibit the phase shift and a simple function of the wave amplitude plotted vs. the source-detector separation. From the slopes of these linear position-dependent measurements, one can deduce the wavelength of the disturbance, as well as the absorption and scattering factors of the homogeneous turbid medium via Equations 21.3 and 21.4.

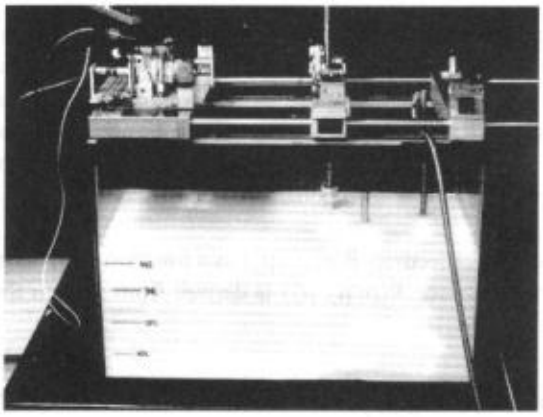

A

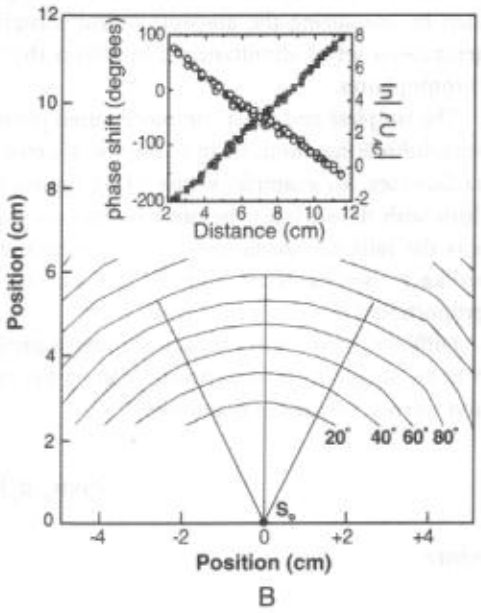


B

**FIGURE 21.2** (A) An aquarium used for model experiments. The aquarium is filled with Intralipid, a polydisperse emulsion whose absorption and scattering coefficients in the NIR region can be adjusted to approximate those of tissue. (B) Constant-phase contours of diffuse photon-density waves in the homogeneous sample of Intralipid. The source for this measurement is a 1-mW laser diode operating at 780 nm and modulated at 200 MHz. Inset: Measured phase-shift and a dimensionless (logarithmic) function of the amplitude as a function of source-detector separation.

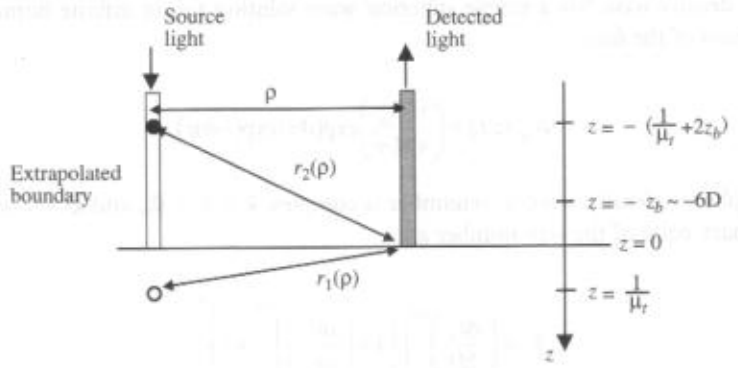


**FIGURE 21.3** Schematic of the experimental fiber configuration showing the relative positions of surface boundary ($z = 0$), extrapolated boundaries, $r_1(\rho)$ and $r_2(\rho)$ as defined in Equations 21.5, 21.6a, and 21.6b.

For homogeneous media in more complex geometries, one can still derive a set of phase and amplitude curves as a function of source-detector separation. The functional relationships may not be linear, but it is still readily possible to derive the average absorption and scattering factors of the underlying media by fitting to this data.

### 21.2.4 Spectroscopy of Homogeneous Turbid Media

The absorption factor, $\mu_a$, depends on the chromophore concentrations, and their extinction coefficients. The predominant endogenous absorbers in tissues are oxy- and deoxyhemoglobin, and water. The scattering factor, $\mu_s'$, depends on other tissue properties such as organelle (e.g., mitochondria) concentration and the index of refraction of the background fluids. If the medium is sufficiently homogenous, then by measuring the absorption and scattering coefficients as a function of light wavelength, one generates a set of simultaneous equations that can be solved to yield the concentrations of the tissue chromophores.

The simplest and most commonly used physical model for tissue spectroscopy treats the sample as a semi-infinite medium. In this case the sources and detectors are placed on the "air side" of the tissue surface (see, for example, Figure 21.3). Emission and detection take place through optical fibers placed flush with the surface. The quantity measured in practice at position **r**, time $t$, and along the direction $n$ is the radiance integrated over the collection solid angle. Within the diffusion approximation, the radiance consists of an isotropic fluence rate ($\Phi(\mathbf{r},t)$) and a directional photon flux ($J(\mathbf{r},t)$) that is proportional to the gradient of $\Phi$.

Diffusion theory for semi-infinite media predicts the reflectivity $R(\rho; \mu_a, \mu_s')$ as a function of $\rho$, where $\rho$ is the source-detector separation along the sample surface. $R(\rho; \mu_a, \mu_s')$ is derived from photon flux and fluence rate at the boundary[79,80]

$$R(\rho;\mu_a,\mu_s') = C_1\Phi(\rho) + C_2 J_z(\rho) \tag{21.5}$$

where

$$\Phi(\rho) = \frac{1}{4\pi D}\left(\frac{\exp(-\mu_{eff} r_1(\rho))}{r_1(\rho)} - \frac{\exp(-\mu_{eff} r_2(\rho))}{r_2(\rho)}\right) \tag{21.6a}$$

and

$$J_z(\rho) = \frac{1}{4\pi\mu_t}\left[\left(\mu_{eff} + \frac{1}{r_1(\rho)}\right)\frac{\exp\left(-\mu_{eff} r_1(\rho)\right)}{r_1^2(\rho)}\right. \\ \left. + \left(\frac{1}{\mu_t} + 2z_b\right)\left(\mu_{eff} + \frac{1}{r_2(\rho)}\right)\frac{\exp\left(-\mu_{eff} r_2(\rho)\right)}{r_2^2(\rho)}\right] \quad (21.6b)$$

Here, $\mu_t = \mu_a + \mu_s'$, and $\mu_{eff} = [3\mu_a(\mu_a + \mu_s')]^{1/2}$. $C_1$ and $C_2$ are constants that depend on the relative refractive index mismatch between the tissue and the detector fiber, and the numerical aperture of the detection fibers. The parameters $r_i(\rho)$ are defined in Figure 21.2. Briefly, $r_1(\rho)$ is the distance from the point of contact of the detector fiber on the tissue surface to the effective source position in the tissue located $1/\mu_t'$ directly beneath the source fiber; $r_2(\rho)$ is the distance between the point of contact of the detector fiber and a point located $1/\mu_t + 2z_b$ directly above the source; $z_b$ is the extrapolated boundary length above the surface of the medium. Here the $z$-direction has been taken normal to the tissue surface (located at $z = 0$), so that $J_z$ is the directional flux normal to the surface.

The tissue optical properties at a fixed wavelength are derived from the measured reflectance by fitting with Equation 21.5. Many schemes have been developed to search for the optimal parameters;[80–82] their relative success depends on the measurement signal-to-noise ratio and the accuracy of the physical model. When everything works, one obtains a best estimate of the absorption factor and scattering factor at one or more optical wavelengths. We then decompose the absorption coefficient into contributions from different tissue chromophores, i.e.,

$$\mu_a(\lambda) = \sum_i \varepsilon_i(\lambda)\, c_i \,. \quad (21.7)$$

Here the sum is over the different tissue chromophores; $\varepsilon_i(\lambda)$ is the extinction coefficient as a function of wavelength for the $i$th chromophore and $c_i$ is the concentration of the $i$th chromophore. The $c_i$ are unknowns to be reconstructed from the wavelength-dependent absorption factors. Three unknowns require measurements at a minimum of three optical wavelengths (generally more, because tissue scattering is also an unknown).

Oxy- and deoxyhemoglobin concentrations (e.g., $c_{HbO_2}$, $c_{Hb}$, respectively) along with water concentration are the most significant tissue absorbers in the NIR. They can be combined to obtain blood volume (which is proportional to total hemoglobin concentration ($[c_{Hb} + c_{HbO_2}]$) and blood oxygen saturation (i.e., $[c_{HbO_2}/(c_{Hb} + c_{HbO_2})] \times 100$), which in turn provide useful physiological information. The same schemes are often extended to derive information about exogenous agents such as photodynamic therapy (PDT) drugs, indocyanine green (ICG), etc.; in such cases the effect of these other chromophores is accounted for by adding their contribution to the sum in Equation 21.7.

## 21.2.5 Imaging in Heterogeneous Media

### 21.2.5.1 Brief History

Tissue is often quite heterogeneous, so it is natural to contemplate making images with the diffusive waves. While high spatial resolution is desirable (e.g., a few millimeters), resolutions of about 1 cm are useful for many problems. A simple example of the utility of imaging is the early localization of a head injury that causes brain bleeding or hematomas. Tumors are another type of structural anomaly that one wants to detect, localize, and classify. The diffuse optical methods probe a variety of properties associated with tumor growth: larger blood volume resulting from a larger number density and volume fraction of blood vessels residing within the tumor; blood deoxygenation arising from relatively high metabolic activity within the tumor; increased concentration of the intracellular organelles necessary for the energy production associated with rapid growth; and the accumulation of highly scattering calcium precipitates.

Some of these properties may prove helpful in classifying tumors as benign or malignant. In the long term it should be possible to design contrast agents that respond to specific tumor properties. Other types of tissue of interest for functional imaging include the neonatal brain and a variety of animal models. For example, physiological studies of hemodynamics in relation to the oxygen demand probe important changes in the functional brain, especially during mental activity. In Section 21.4 we describe current research that investigates many of the clinical issues just outlined.

Optical characterization of the heterogeneous tissues has been attempted since 1929[83] when the term *diaphanography* was applied to shadowgraphs of breast tissue. This class of transillumination measurement was renewed in the early 1980s.[84–95] Even in the region of low tissue absorption, however, the high degree of tissue scattering distorted spectroscopic information and blurred optical images as a result of the large distribution of photon pathways through the tissue. Widebeam transillumination proved largely inadequate for clinical use because the two-dimensional "photographic" data were poorly suited for image reconstruction. The mathematical modeling of light transport in tissues was not developed sufficiently for optical tomography to be readily employed.

The diffusion approximation now provides a tractable basis for tomographic approaches to image reconstruction using highly scattered light. Tomographic methods crucial for recovery of information about breast heterogeneities were not employed in the early transillumination patient studies. Several approaches have been developed for diffuse optical tomography; these include: backprojection methods,[96,97] diffraction tomography in $k$-space,[98–101] perturbation approaches,[102–107] the Taylor series expansion approach,[108–113] gradient-based iterative techniques,[114] elliptic systems method (ESM),[115,116] and Bayesian conditioning.[117] Backprojection methods, borrowed from CT, produce images quickly and use few computational resources. However, they lack quantitative information and rely on simple geometries. Perturbation approaches based on Born or Rytov approximations can use analytic forms or iterative techniques based on numerical solutions. The analytic forms are relatively fast, but require the use of simple boundary conditions and geometries, and generally underestimate the properties of the perturbations. The numerical solutions are relatively slow and computationally intensive; however, in principle, realistic boundaries present no significant limitations for these methods.

### 21.2.5.2 Formulation of the Imaging Problem

In this section we formulate the imaging problem in the frequency domain. The starting point of this analysis is the time-independent form of the diffusion equation (Equation 21.1), where we have divided out all of the $e^{i\omega t}$ dependencies:

$$\nabla \cdot D(\mathbf{r})\nabla\Phi(\mathbf{r}) - \left(v\mu_a(\mathbf{r}) - i\omega\right)\Phi(\mathbf{r}) = -vS(\mathbf{r},\omega)\,. \tag{21.8}$$

The problem is difficult because the diffusion coefficient and the absorption coefficient vary with spatial position. We write $D(\mathbf{r}) = D_o + \delta D(\mathbf{r})$, and $\mu_a(\mathbf{r}) = \mu_{ao} + \delta\mu_a(\mathbf{r})$; here $D_o$ and $\mu_{ao}$ are constant, "background" optical properties. The source can have any form, but typically we assume point sources of the form $A\delta(\mathbf{r} - \mathbf{r}_s)$.

The goal of diffuse optical imaging is to derive $D(\mathbf{r})$ and $\mu_a(\mathbf{r})$ from measurements of $\Phi(\mathbf{r})$ on the sample surface. Two common forms are used for $\Phi(\mathbf{r})$ in the formulation of the inversion problem. The Born-type approach writes $\Phi(\mathbf{r}) = \Phi_o(\mathbf{r}) + \Phi_{sc}(\mathbf{r})$; traditionally one can view $\Phi_o(\mathbf{r})$ as the incident wave and $\Phi_{sc}(\mathbf{r})$ as the wave produced by the scattering of this incident wave off the absorptive and diffusive heterogeneities. The Rytov approach writes $\Phi(\mathbf{r}) = \Phi_o(\mathbf{r})\exp[\Phi_{sc}(\mathbf{r})]$. We will focus on the Born approximation for our analysis, and indicate when possible the corresponding Rytov results.

We next substitute $D(\mathbf{r})$, $\mu_a(\mathbf{r})$, and $\Phi(\mathbf{r}) = \Phi_o(\mathbf{r}) + \Phi_{sc}(\mathbf{r})$ into Equation 21.8 to obtain a differential equation for $\Phi_{sc}(\mathbf{r})$ with general solution:

$$\Phi_{sc}(\mathbf{r}_d,\mathbf{r}_s) = \int\left(\frac{-v\delta\mu_a(\mathbf{r})}{D_o}\right)G(\mathbf{r}_d,\mathbf{r})\Phi(\mathbf{r},\mathbf{r}_s)d\mathbf{r} + \int\left(\frac{\delta D(\mathbf{r})}{D_o}\right)\nabla G(\mathbf{r}_d,\mathbf{r})\cdot\nabla\Phi(\mathbf{r},\mathbf{r}_s)d\mathbf{r}\,. \tag{21.9}$$

Here $\mathbf{r}_s$ is the source position, $\mathbf{r}_d$ is the detector position, $\mathbf{r}$ is a position within the sample. The integration is over the entire sample volume. $G(\mathbf{r},\mathbf{r}')$ is the Green's function associated with Equation 21.8. Examination of Equation 21.9 reveals some of the intrinsic challenges of the inverse problem. In a typical experiment one measures $\Phi$ on the sample surface and then extracts $\Phi_{sc}$ on the surface by subtracting $\Phi_o$ from $\Phi$. The problem of deriving $\delta\mu_a(\mathbf{r})$ and $\delta D(\mathbf{r})$ from $\Phi$ is intrinsically nonlinear because $\Phi$ and $G$ are nonlinear functions of $\delta\mu_a(\mathbf{r})$ and $\delta D(\mathbf{r})$.

***The Linearized Problem***

The simplest and most direct route to inverting Equation 21.9 starts by replacing $\Phi$ by $\Phi_o$ and $G$ by $G_o$. Here $\Phi_o$ and $G_o$ are solutions of the homogeneous version of Equation 21.8 with $D(\mathbf{r}) = D_o$, and $\mu_a(\mathbf{r}) = \mu_{ao}$. This approximation is good when $\Phi_o << \Phi$, and when the perturbations are very small compared to the background. It is also important that we have accurate estimates of $D_o$ and $\mu_{ao}$. In this case, Equation 21.9 is readily discretized in Cartesian coordinates and written in the following form:

$$\Phi_{sc}(\mathbf{r}_d,\mathbf{r}_s) = \sum_{j=1}^{NV}\left(W_{a,j}\delta\mu_a(\mathbf{r}_j) + W_{s,j}\delta D(\mathbf{r}_j)\right). \tag{21.10}$$

The sum is taken over $NV$ volume elements (i.e., voxels) within the sample; the absorption and scattering weights are, respectively, $W_{a,j} = G_o(\mathbf{r}_d,\mathbf{r}_j)\,\Phi_o(\mathbf{r}_j,\mathbf{r}s)\,(-v\Delta x\,\Delta y\,\Delta z/D_o)$, and $W_{s,j} = \nabla G_o(\mathbf{r}_d,\mathbf{r}_j)\cdot\nabla\Phi_o(\mathbf{r}_j,\mathbf{r}_s)\,(\Delta x\,\Delta y\,\Delta z/D_o)$. In any practical situation there will be $NS$ sources and $ND$ detectors, and so there will be up to $NM = NS \times ND$ measurements of $\Phi$ on the sample surface. For the multisource-detector problem one naturally transforms Equation 21.10 into a matrix equation, i.e.,

$$\left[\mathrm{W}_{a,ij},\mathrm{W}_{s,ij}\right]\left\{\delta\mu_a(\mathbf{r}_j),\delta D(\mathbf{r}_j)\right\}^T = \left\{\Phi_{sc}(\mathbf{r}_d,\mathbf{r}_s)_i\right\}. \tag{21.11}$$

Here, the index $i$ refers to source-detector pair, and the index $j$ refers to position within the sample. The perturbation vector $\{\delta\mu_a(\mathbf{r}_j), \delta D(\mathbf{r}_j)\}^T$ is $2NV$ in length, the measurement vector $\{\Phi_{sc}(\mathbf{r}_d,\mathbf{r}_s)_i\}$ is $NM$ in length, and the matrix [W] has dimensions $NM \times (2NV)$. In the Rytov scheme, the formulation in the weak perturbation limit is almost exactly the same, except that $W_{a,ij} = G_o(\mathbf{r}_d,\mathbf{r}_j)\,\Phi_o(\mathbf{r}_j,\mathbf{r}_s)(-v\Delta x\,\Delta y\,\Delta z/\Phi_o(\mathbf{r}_d,\mathbf{r}_s)\,D_o)$, $W_{s,j} = \nabla G_o(\mathbf{r}_d,\mathbf{r}_j)\cdot\nabla\Phi_o(\mathbf{r}_j,\mathbf{r}_s)\,(\Delta x\,\Delta y\,\Delta z/\Phi_o(\mathbf{r}_d,\mathbf{r}_s)\,D_o)$, and the vector $\{\Phi_{sc}(\mathbf{r}_d,\mathbf{r}_s)_i\}$ is set equal to $\{\ln[\Phi(\mathbf{r}_d,\mathbf{r}_s)/\Phi_o(\mathbf{r}_d,\mathbf{r}_s)]_i\}$ rather than $\{[\Phi(\mathbf{r}_d,\mathbf{r}_s) - \Phi_o(\mathbf{r}_d,\mathbf{r}_s)]_i\}$. The Rytov scheme has some experimental advantages because it is intrinsically normalized (the Born scheme, however, can be modified so that it is normalized in essentially the same way); the major approximations of the Rytov scheme are associated with the gradients of $\Phi$, in particular that $(\nabla\Phi_{sc})^2$ is small relative to the perturbation terms in Equation 21.9. Thus both Born and Rytov approaches give rise to an inverse problem of the form [W] $\{x\} = \{b\}$; the unknown vector $\{x\}$ can be determined from this set of linear equations by a number of standard mathematical techniques. The numerical elements in [W] are often assigned in simple geometries using analytic forms of $G_o$ and $\Phi_o$ (e.g., Equation 21.3 and variants), or more generally by numerically solving Equation 21.8 and its Green's function analog for $\Phi_o$ and $G_o$.

***The Nonlinear Problem***

The linear formulation described above works well when perturbations are small and isolated, and when the background media are relatively uniform. However, Equation 21.9 is intrinsically nonlinear because $\Phi$ and $G$ are also functions of the variables we are trying to determine by inversion. The most broadly useful image reconstruction schemes are iterative. These approaches follow similar algorithms: (1) the optical properties ($\mu_a$ and $D$) are initialized; (2) the forward problem is solved; (3) a chi-squared is calculated and convergence is checked; (4) the inverse problem is set up; (5) the inverse problem is solved; (6) the optical properties are updated and a return to step 1 occurs.

The forward problem is defined as calculating the diffuse photon density, $\Phi_C(\mathbf{r},\mathbf{r}_s)$, for each source position $\mathbf{r}_s$ and is typically found using finite elements or finite difference methods using Equation 21.8. The boundary conditions are defined as:

$$\frac{\partial \Phi_C}{\partial \hat{n}} = -\alpha \Phi_C, \quad \alpha = \frac{(1 - R_{eff})}{(1 + R_{eff})} \frac{3\mu_s'}{2}. \tag{21.12}$$

$R_{eff}$ is the effective reflection coefficient and can be approximated by: $R_{eff} = -1.440n^{-2} + 0.710n^{-1} + 0.668 + 0.0636n$, $n = n_{in}/n_{out}$ the relative index of refraction.[55] The chi-squared ($\chi^2$) is generally defined as:

$$\chi^2 = \sum_{NM} \left( \frac{\Phi_M(r_d^i) - \Phi_C(r_d^i)}{\sigma^i} \right)^2. \tag{21.13}$$

Here $NM$ = number of measurements, $M$ = measured, $C$ = calculated, $\mathbf{r}_d^i$ is the $i$th detector position, and $\sigma^i$ is the $i$th measurement error. By comparing $\chi^2$ to some defined $\varepsilon$, a convergence criterion is defined and checked.

We then need a way of updating the optical properties from their previous values. A standard Taylor method expands $\Phi_C$ about its assumed optical property distribution, which is a perturbation away from another distribution presumed closer to the true value. In particular we set the measured photon density wave for each source-detector pair equal to the calculated photon density wave at the corresponding source-detector pair plus the first-order Taylor series perturbation expansion terms in $\mu_a$ and $D$, i.e., $\Phi_M = \Phi_C + (\partial \Phi_C/\partial \mu_a)\Delta\mu_a + (\partial \Phi_C/\partial D)\Delta D$.

The inverse problem is defined from this relationship:

$$[J]\{\Delta\mu_a, \Delta D\}^T = -\{\Phi_M(\mathbf{r}_d) - \Phi_C(\mathbf{r}_d)\}. \tag{21.14}$$

Here $[J] = [\partial \Phi_C/\partial \mu_a, \partial \Phi_C/\partial D]$ is called the Jacobian. The Jacobian matrix will have the following entries:

$$\left[ \frac{\partial \Phi_C}{\partial \mu_a} \right]_{ij} = \frac{-v\Delta x \Delta y \Delta z}{D_o} G(\mathbf{r}_{di}, \mathbf{r}_j) \Phi_C(\mathbf{r}_j, \mathbf{r}_{si}) \tag{21.15a}$$

$$\left[ \frac{\partial \Phi_C}{\partial D} \right]_{ij} = \frac{\Delta x \Delta y \Delta z}{D_o} \nabla G(\mathbf{r}_{di}, \mathbf{r}_j) \cdot \nabla \Phi_C(\mathbf{r}_j, \mathbf{r}_{si}). \tag{21.15b}$$

It is illuminating at this point to compare Equation 21.14 with Equation 21.11. The two expressions are essentially the same if we associate $\Phi_M$ with $\Phi$, $\Phi_C$ with $\Phi_o$, $\Delta\mu_a$ with $\delta\mu_a$, $\Delta D$ with $\delta D$, and if we use the true Green's function $G$ rather than $G_o$. The same set of substitutions in the Rytov formulation gives a Rytov version of the nonlinear inversion scheme. Thus the iterative formulation of the inverse problem is based on the same underlying integral relationship (Equation 21.9), and one readily sees that each step of the "nonlinear" iteration process is a linear inverse problem of the form [J] {x} = {b}.

### 21.2.5.3 Methods for Solving the Inverse Problem

The inverse problem may be solved using a wide range of methods (an excellent review of these methods was given by Arridge[118]). The solution method chosen depends in part on the determination of the *implicit* or *explicit* Jacobian. For the explicit Jacobian two methods are commonly employed: the Newton-Raphson and the conjugate gradient techniques. It is also possible to combine these methods with Bayesian conditioning or regularization to improve reconstruction. For the implicit Jacobian, the methods of choice are the gradient-based iterative technique and ART (algebraic reconstruction technique).

There are essentially two ways to construct the Jacobian, [J] *explicitly*: direct and adjoint. The *direct* approach explicitly takes the derivative of the forward problem (Equation 21.8) with respect to the optical properties to determine the Jacobian. For example, suppose [A]{$\Phi_C$} = {S} is the forward problem; here [A] is the operator on the left side of Equation 21.8 and {S} is the source on the right side of Equation 21.8.